# Accepted Manuscript

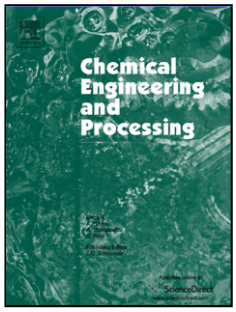


Title: Influencing Selectivity in the Oxidative Coupling of Methane by Modulating Oxygen Permeation in a Variable Thickness Membrane Reactor

Authors: Ojotule P. Onoja, Xiaodong Wang, Panagiotis N. Kechagiopoulos

PII: S0255-2701(18)30995-4
DOI: https://doi.org/10.1016/j.cep.2018.11.016
Reference: CEP 7431

To appear in: *Chemical Engineering and Processing*

Received date: 26 August 2018
Revised date: 21 November 2018
Accepted date: 23 November 2018

Please cite this article as: Onoja OP, Wang X, Kechagiopoulos PN, Influencing Selectivity in the Oxidative Coupling of Methane by Modulating Oxygen Permeation in a Variable Thickness Membrane Reactor, *Chemical Engineering and Processing - Process Intensification* (2018), https://doi.org/10.1016/j.cep.2018.11.016

# Influencing Selectivity in the Oxidative Coupling of Methane by Modulating Oxygen Permeation in a Variable Thickness Membrane Reactor

Ojotule P. Onoja, Xiaodong Wang, Panagiotis N. Kechagiopoulos*

Chemical and Materials Engineering Group, School of Engineering, University of Aberdeen, Aberdeen, AB24 3UE, UK

* **Corresponding author**: p.kechagiopoulos@abdn.ac.uk

## Graphical abstract

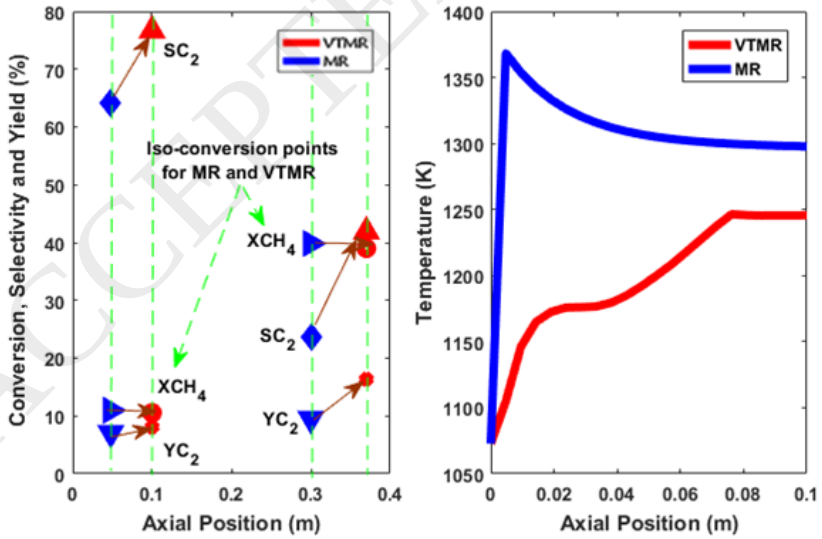

**Highlights:**

- Variable thickness membrane reactor (VTMR) concept proposed for OCM
- Higher $C_2$ selectivity achieved over normal membrane reactors at equal conversions
- Hotspot formation likelihood minimised significantly through axial $O_2$ modulation
- Gas phase reactions and radial diffusion found as main $C_2$ selectivity loss factors
- Oxygen permeation limited by reactor side surface kinetics on thin dense membranes

## Abstract

The Oxidative Coupling of Methane (OCM) has been considered for years as a promising alternative for the production of higher hydrocarbons, namely ethane and ethylene. Nonetheless, OCM's inherent conversion-versus-selectivity limitations have not allowed till now for economical C2 yields to be achieved. Reactor engineering studies guided by a detailed mechanistic description of the reaction can directly contribute to obtaining an understanding of these limitations. In this work, a Variable Thickness Membrane Reactor (VTMR) is proposed, wherein O2 permeation along the reactor is modulated, aiming at maximizing C2 selectivity. 1D and 2D reactor simulations are carried out to compare the performance of this reactor to conventional co-feed Packed Bed Reactors (PBR) and Membrane Reactors without variable thickness (MR). Particular attention is given on the impact of gas phase reactions on C2 selectivity, while the effect of surface exchange kinetics on both sides of the membrane and bulk diffusion of O2 across the membrane is discriminated. When identical operating conditions (T = 1073 K, P = 1 atm, Space time = 7.85 s) and reactor geometry (Length = 0.1 m, Diameter = 0.01 m) were evaluated, the optimization performed of the VTMR configuration achieved a $C_2$ selectivity of 67.26 %, in comparison to 47.86 % and 29.87 % for the MR and PBR, respectively, highlighting the potential of the concept.

**Keywords:** Variable thickness membrane reactor, $C_2$ selectivity, Gas phase reactions, Oxidative coupling of methane

# 1 Introduction

Ethylene is the most widely produced organic commodity in the chemical industry with an annual global demand of over $140\times10^6$ tons and a growth rate of 3.5 % per year [1]. However, being produced via steam cracking of naphtha, or other hydrocarbons, its availability is directly linked to that of the fast diminishing crude oil resources. Ethylene production via the single step Oxidative Coupling of Methane (OCM) is a promising and less energy intensive process, which can also break the crude oil dependency. However, OCM is characterized by a trade-off between achieving high (low) $C_2$ selectivity at conditions where $CH_4$ conversion is low (high), resulting in non-economical $C_2$ yields [2]. Since the pioneering work of Keller and Bhasin [3] and despite extensive research in OCM catalysis, only the recently developed nanowire catalysts by Siluria Technologies have managed to bring closer the commercial realization of OCM [4,5]. A need for novel reactor design that minimizes the inherent $C_2$ yield limitations of OCM is, hence, imperative, and highly economically and environmentally relevant [6].

High $C_2$ selectivity can be achieved at high $CH_4/O_2$ ratios that avoid deep oxidation routes [7]. As such, membrane reactors, providing a controlled $O_2$ dosing, have long been envisaged as a promising OCM reactor configuration [8]. High permselectivity dense membranes avoid the expensive $O_2$ separation step from air, however the low permeation flux limits the reactor's productivity [9–12]. Mixed ionic/electronic conducting (MIEC) dense membranes of perovskite structure have attracted particular research interest on account of their suitable for OCM operating temperature range at around 800$^o$C [13,14]. Porous membranes show a higher flux, but that can impact negatively on $C_2$ selectivity, while back diffusion from the low to the higher pressure side cannot be excluded [6,15–17]. Supporting a thin dense layer on variable porosity and pore size porous layers [10] has made it possible to achieve higher $O_2$ fluxes, while maintaining a high permselectivity. The work of Othman et al. [10] in a hollow fiber

membrane microreactor reporting a very high $C_2$ yield of 39 % is a prime example of the potential of such configurations.

Nonetheless, membrane reactors are still reported to be limited by the formation of hotspots and high pressure drop, while most promising results have been typically obtained using dilute feeds [18]. Moreover, high $O_2$ availability towards the reactor end can still have an adverse effect on $C_2$ selectivity [18]. To decrease secondary $C_2$ oxidation, Godini et al. [6] used a modified porous membrane with decreasing $O_2$ permeation, reporting a 25.8 % $C_2$ yield and 66 % $C_2$ selectivity. The use of distributed or staged $O_2$ feeding has also been considered for other processes, such as autothermal steam reforming of methane [19–22], although primarily aiming at optimal temperature control. Aworinde et al. [2] further showed selectivity improvements via the simultaneous modulation of $O_2$ and coolant temperature for the preferential oxidation of o-xylene to phthalic anhydride.

Modelling studies can greatly contribute in assessing the performance of such novel reactor concepts and assist in determining their optimal design characteristics. Reported work has compared reactor configurations [23,24] proposed feeding policies [25] and conducted optimization of operating conditions [26]. In membrane tubular reactors, the inherent radial component, brought about by the perpendicular introduction of $O_2$, has underlined the need for considering 2D models to correctly describe experimental results [27]. In conventional co-feed packed bed reactors, the high reactivity of radicals involved in gas phase reactions was found critical to account for in pellet-scale intraparticle and interstitial gradients [28], and was revealed to even impact on intraparticle surface species coverages and, consequently, reactor performance [29]. Nonetheless, such advanced (micro-) kinetic modelling approaches have not been applied to membrane reactor configurations.

The productivity of OCM membrane reactors depends clearly on the amount of $O_2$ in the catalytic side, however the latter affects both the coupling and combustion reactions, so controlling $O_2$ permeation through the membrane is imperative [6]. In this study, an OCM membrane reactor with a MIEC membrane of varying thickness that allows tuning the $O_2$ partial pressure across the reactor is proposed (Figure 1). The concept's potential towards improved performance is investigated computationally and compared with conventional membrane and packed bed reactors, using 1D and 2D reactor model representations. Gas phase microkinetics are considered to properly account for the effect of homogeneous radical reactions, while attention is further given on discriminating the impact of the membrane's variable thickness on bulk ionic transport versus surface-exchange reactions. An overall optimization of the membrane design is carried out leading to enhanced $C_2$ selectivity.

## 2 Procedures

### 2.1 Reactor model

A membrane reactor of shell-and-tube geometry is assumed for the simulations, a schematic of which is presented in Figure 1. Methane is fed to the tube side that is packed with OCM catalyst, while air is fed cocurrently to the shell side of the reactor. Mass and heat balances are derived for both reaction (tube) and air (shell) sides. 2D and 1D descriptions are implemented to investigate the effect of external radial concentration and temperature gradients in the reaction side. Criteria by Mears [30], Smith [31] and Weisz [32] in relation to the importance of axial dispersion, radial velocity gradients and intraparticle transport limitations were evaluated and found valid for the simulated reactor geometry and catalyst pellet dimensions. Additionally, pressure drop was evaluated via the Ergun equation and was negligible in all simulated cases.

Based on the above and in order for the pertinent performance differences between reactor concepts to be able to be elucidated, the developed models assume ideal gas behaviour and

steady state operation under isobaric conditions, while longitudinal dispersion and internal mass and heat transfer resistances are considered negligible. No reactions are considered to take place in the membrane itself, which is modelled through its contribution to mass and energy balances via the permeation flux terms $J_i$.

The respective mass and energy balances for the 2D (equations (1) and (2)) and 1D (equations (3) and (4)) cases in the tube side are given below:

$$U_{z,t}\frac{\partial C_{i,t}}{\partial z} = D_{er}\left(\frac{\partial^2 C_{i,t}}{\partial r^2} + \frac{1}{r}\frac{\partial C_{i,t}}{\partial r}\right) + \sum_j R_{ij} \quad (1)$$

$$U_{z,t}\sum_i\left(c_{pi,t}C_{i,t}\right)\frac{\partial T_t}{\partial z} = \lambda_{er}\left(\frac{\partial^2 T_t}{\partial r^2} + \frac{1}{r}\frac{\partial T_t}{\partial r}\right) + \sum_j(-\Delta H_{R_j}R_j) \quad (2)$$

$$U_{z,t}\frac{dC_{i,t}}{dz} = \sum_j R_{ij} + \frac{4}{d_t}J_i \quad (3)$$

$$U_{z,t}\sum_i\left(c_{pi,t}C_{i,t}\right)\frac{dT_t}{dz} = \sum_j(-\Delta H_{R_j}R_j) - \frac{4}{d_t}\left[U_a + \sum_i\left(c_{pi,t}J_i\right)\right](T_t - T_s) \quad (4)$$

For both 2D and 1D cases above, a plug flow 1D representation is used for the shell side mass and energy balance:

$$U_{z,s}\frac{dC_{i,s}}{dz} = -\frac{4}{d_t}J_i \quad (5)$$

$$U_{z,s}\sum_i\left(c_{pi,s}C_{i,s}\right)\frac{dT_s}{dz} = \frac{4}{d_t}\left[U_a + \sum_i\left(c_{pi,s}J_i\right)\right](T_t - T_s) \quad (6)$$

The corresponding inlet and boundary conditions, assuming axial symmetry under cylindrical coordinates for the reaction side in the 2D case, are given below. In the case of 1D simulations, only equation (7) is relevant.

$$z = 0: \quad C_{i,t} = C_{i,t0}, \quad C_{i,s} = C_{i,s0}, \quad T_t = T_s = T_0 \quad (7)$$

$$r = 0: \quad \frac{\partial C_{i,t}}{\partial r} = 0, \quad \frac{\partial T_t}{\partial r} = 0 \quad (8)$$

$$r = \frac{d_t}{2}: \quad D_{er}\frac{\partial C_{i,t}}{\partial r} = J_i, \quad \lambda_{er}\frac{\partial T_t}{\partial r} = \left[\alpha_w + \sum_i\left(c_{pi,t}J_i\right)\right](T_t - T_s) \quad (9)$$

The components $i$ for which the above mass balances are solved depend on the reaction network considered as will be further explained in the following section. Since oxygen conducting dense membranes are considered, it follows that $J_i = 0$ for $i \neq O_2$, hence the above balances and respective boundary equations hold both for $O_2$ and for all the components that do not permeate.

Co-feed packed bed reactor (PBR) simulations are also conducted for comparison, where 1D and 2D representations are derived as above, but excluding any mass and heat transfer flows between the shell and the tube sides. Essentially, the 1D PBR was simulated using equations (3) and (4), substituting $J_i = U_a = 0$, while the 2D PBR was simulated using equations (1) and (2), but substituting at the boundary equations (8) and (9) $J_i = a_w = 0$. In both cases only the relevant tube side initial conditions from equation (7) were considered, namely $C_{i,t} = C_{i,t0}$ and $T_t = T_0$. The partial differential equations (PDE) system describing the mass and energy balances and the corresponding boundary conditions for the 2D case (equations (1), (2) and (5)-(9)) are discretized in the radial dimension using a central finite differences scheme. The resulting differential-algebraic equations (DAE) system is solved using a DDASSL-based integrator within the Athena Visual Studio software. The 1D ordinary differential equations (ODE) system comprising of equations (3)-(7) is solved following equivalent procedures. For the calculation of the effective radial diffusivity and conductivity, overall heat transfer coefficient and wall heat transfer coefficient, appearing in the above equations, relevant procedures are given in the Supporting Information (SI).

### 2.2 Kinetic model

A 10-step kinetic model is adopted from Stansch et al. [33] to describe the OCM heterogeneous-homogeneous chemistry over a $La_2O_3$/CaO catalyst. The model assumes 3 primary catalytic reaction steps to describe the oxidative conversion of $CH_4$ towards $CO_2$, $C_2H_6$ and CO, while secondary catalytic steps account for the oxidative dehydrogenation of $C_2H_6$ to

$C_2H_4$, the conversion of $C_2H_4$ to CO via partial oxidation and steam reforming and the conversion of CO to $CO_2$ via direct oxidation and the water gas shift reaction. Hougen-Watson type of equations are utilized to express the rate of catalytic reactions involving $O_2$, accounting for the inhibiting effect of $O_2$ and/or $CO_2$, while power law expressions are used for the remaining reactions. The model assumes only one global gas-phase reaction, the thermal dehydrogenation of $C_2H_6$ to $C_2H_4$, indicated in the following as gas phase model GM-1. When simulations with GM-1 are carried out, the mass balances of Section 2.1 are solved for 9 molecules: $CH_4$, $O_2$, CO, $CO_2$, $C_2H_6$, $C_2H_4$, $H_2$, $H_2O$ and $N_2$. To further investigate the effect of homogeneous reactions in this work, a multi-step gas-phase microkinetic model by Chen et al. [34] is also coupled with the catalytic part of the kinetic model by Stansch et al. [33], substituting in certain simulation cases the simple GM-1 model. This microkinetic model, indicated as gas phase model GM-2, comprises of 38 reversible reactions between 13 molecules ($H_2$, $H_2O$, $H_2O_2$, $O_2$, $CH_4$, $CH_2O$, CO, $CO_2$, $C_2H_2$, $C_2H_4$, $C_2H_6$, $C_3H_6$ and $C_3H_8$) and 10 radicals (H·, O·, OH·, $HO_2$·, CHO·, $CH_3O$·, $CH_3$·, $C_2H_3$·, $C_2H_5$· and $C_3H_7$·), so in the case of simulations with GM-2 mass balances of Section 2.1 are solved for these 23 species plus $N_2$. Forward rates are calculated via Arrhenius expressions and the law of mass action, whereas reverse direction rate constants are calculated via equilibrium and forward rate constants. Further details on the kinetic parameters of both models (activation energies, frequency factors, reaction orders, etc.) and their assumptions can be found in the respective publications [33,34].

### 2.3 Oxygen permeation flux

Within the proposed concept of using variable thickness MIEC membranes of perovskite structure with high electronic conductivity, alternative expressions for the $O_2$ permeation flux from the shell to the tube side of the reactor are evaluated. Focus is particularly placed on discriminating the involved processes, namely surface exchange kinetics versus diffusion in the bulk. A correlation for $La_{1-x}A'_xFe_{0.8}Co_{0.2}O_{3-\delta}$ perovskite membranes developed by Tsai

et al. [35] based on the assumption that $O_2$ permeation is limited by the diffusion of oxygen vacancies in the bulk oxide is first considered (denoted as flux model $JO_2$-1):

$$J_{O_2} = Ae^{-\frac{E_a}{RT}} \frac{T_{avg}}{L_m} \ln\left(\frac{P_{O_2,s}}{P_{O_2,t}}\right) \quad (10)$$

In this work, equation (10) is parameterized based on the values obtained by Tsai et al. [35] for $A'_x = Ba_{0.8}$, since this formulation showed the highest permeation rate out of all materials tested in that work (see Table S1 in SI and original publication [35] for activation energies, pre-exponential factors values and further details).

Secondly, a more rigorous permeation flux expression developed by Xu et al. [36] for $La_{0.6}Sr_{0.4}Fe_{0.8}Co_{0.2}O_{3-\delta}$ perovskite membranes and accounting for bulk ionic diffusion and surface exchange reactions at both sides of the membrane is considered. Specifically, an adaptation of this model, which was originally developed for planar membranes, is used after modifications related to the consideration of cylindrical geometry membranes [37,38] (denoted as flux model $JO_2$-2):

$$J_{O_2} = \frac{\frac{k_r}{k_f}\left(P_{O_2,t}^{-0.5} - P_{O_2,s}^{-0.5}\right)}{\left(\frac{d_t}{d_m} \frac{1}{k_f P_{O_2,t}^{0.5}}\right) + \frac{2L_m}{D_v} + \left(\frac{(d_t+L_m)}{d_m} \frac{1}{k_f P_{O_2,s}^{0.5}}\right)} \quad (11)$$

Equation (11) indicates that the resistance to permeation due to bulk diffusion depends on the membrane thickness and is an intrinsic property of the material. Resistances related to surface kinetics on the $O_2$-rich (shell) and $O_2$-lean (tube) side of the membrane are directly correlated to the partial pressures of $O_2$ on the respective side. If any of these three resistances becomes rate limiting, the respective term in the denominator becomes dominant and simplified forms of equation (11) can be derived (see [36] for details and Table S2 in SI for values needed for parameterization of the equation).

In both flux equations, the membrane thickness is constant for MR simulations or is assumed a linear function of the axial position of the reactor *z* for VTMR runs:

$$L_m = L_{m_0}\left(1 + \frac{\sigma \cdot z}{L_z}\right) \quad (12)$$

Mass transfer of $O_2$ from (to) the gas bulk to (from) the surface of the membrane is not accounted for in this work, as experimental investigations have revealed these processes to be insignificant to the overall $O_2$ permeation flux, even at conditions prone to influence gas-solid transfer [39].

### 2.4 Testing conditions and validation of kinetic models

The range of operating conditions used, and catalyst properties chosen are listed in Table 1. These values were selected on the one hand based on typical conditions OCM literature studies have been carried out at and on the other hand following a range of preliminary simulations to select conditions that allowed a fair and clear comparison of the investigated reactor configurations. The reactor geometry and total flow rate were kept constant in all simulated cases, with only the feeding policy of $O_2$ differing among the co-feed and membrane reactors. Specifically, the total amount of $O_2$ that entered the tube side of the MR from the shell with the GM-2 and $JO_2$-1 models was used as the inlet $O_2$ for all PBR simulations. A $N_2$ flow was utilized for the PBR and tube side MR, so that the total flow rate was kept constant, substituting part of $N_2$ with $O_2$ in PBR versus (VT)MR cases where only $CH_4$ and $N_2$ where fed.

Preliminary simulations carried out with the 1D PBR model and using the kinetic model of Stansch et al. [33] with either the GM-1 or GM-2 gas-phase model at a selected set of conditions showed a close agreement with the experimentally reported values (Table S3). Some small deviations using GM-2 at the higher temperatures could indicate a slight underestimation of the contribution of the gas-phase reactions in the work of Stansch et al. [33], however overall the implementation of the kinetic models is deemed valid for the purposes of this work.

### 2.5 Optimization of OCM performance

Optimization of the membrane's axial thickness profile is carried out using a Simulated Annealing (SA) algorithm implemented within Athena Visual Studio aiming at the maximization of the selectivity of $C_2$ species. SA is a random-search optimization technique that performs particularly well at avoiding local optima by accepting not only better solutions but also worse ones (by allowing hill climbing moves) with a given probability [40]. The objective function in terms of a vector of independent variables $\beta$ is given as:

$$\max_{\beta}\left[S_{C_2H_6} + S_{C_2H_4}\right] \tag{13}$$

The DAE or ODE systems defined in Section 2.1 were simulated using the described procedures above during optimization, where the independent variables were allowed to vary between the lower and upper bounds shown in Table 2. These ranges, as well as the initial conditions chosen, were selected based on engineering judgement and available literature data.

### 2.6 Performance parameters

The reactor performance was quantified in all cases considered according to the equations shown below. For the 2D simulation cases the mixing cup method [41] was used to calculate the reported averaged values.

$$CH_4\ \text{Conversion} = 100 \times \frac{F_{CH_{4in}} - F_{CH_{4out}}}{F_{CH_{4in}}}\ \% \tag{14}$$

$$C_2\ \text{Selectivity} = 100 \times \frac{2F_{C_2H_{4out}} + 2F_{C_2H_{6out}}}{F_{CH_{4in}} - F_{CH_{4out}}}\ \% \tag{15}$$

$$C_2\ \text{Yield} = 100 \times \frac{2F_{C_2H_{4out}} + 2F_{C_2H_{6out}}}{F_{CH_{4in}}}\ \% \tag{16}$$

The definition of $O_2$ conversion in a membrane reactor is not evident. In this work, both for MR and VTMR it was calculated by dividing the amount of $O_2$ that reacted in the tube side to

the total amount of $O_2$ that permeated across the membrane according to equation (17). For co-feed PBR $O_2$ conversion was calculated as normal, based on equation (18).

$$O_2\ \text{Conversion}_{(\text{VT})\text{MR}} = 100 \times \frac{2F_{CO_{2\,out}} + F_{CO_{out}} + F_{H_2O_{out}}}{2F_{O_{2\,out}} + 2F_{CO_{2\,out}} + F_{CO_{out}} + F_{H_2O_{out}}}\ \% \quad (17)$$

$$O_2\ \text{Conversion}_{\text{PBR}} = 100 \times \frac{F_{O_{2\,in}} - F_{O_{2\,out}}}{F_{O_{2\,in}}}\ \% \quad (18)$$

Space time appearing in the following sections was defined as the ratio of the total reactor volume over the total volumetric flow rate ($V_R/Q_{tot,0}$), which considering that a homogeneously packed and dispersed catalyst is assumed at a constant bed and catalyst pellet porosity is equivalent to a mass based space time definition.

# 3 Results and discussion

## 3.1 Comparison between PBR and MR

Initially, simulations of a conventional co-feed packed bed reactor (PBR) and a membrane reactor with non-variable membrane thickness (MR) were carried out to provide benchmark performance data for comparison with the proposed variable thickness concept. Isothermal runs are first considered, even though such a mode of operation would be practically challenging for the exothermic OCM, mainly aiming at elucidating the pertinent differences among the reactor configurations before non-isothermal behaviour is accounted for. As will be further discussed in detail, the initial analysis of the simulation data from the various considered reactor models, revealed that a 2D representation is needed to correctly describe all (VT)MR cases, while 1D is sufficient for PBR. As such, in what follows the main focus of the discussion is placed on comparing these cases using the more rigorous kinetic model GM-2, while the rest of the cases are commended when relevant to the discussion. Table 3 summarizes the performance metrics at the same conditions (T = 1073 K, P = 1 atm and $V_R/Q_{tot,0}$ = 7.85 s) for the main cases studied in this and the following sections, while Table S4 in the SI presents the

detailed performance data for all reactor and kinetic models evaluated at these same reference conditions. Further details are given in the respective sections presenting these results.

Results using GM-2 for 1D for PBR and 2D MR with $JO_2$-1 simulations at these reference conditions are shown in Figure 2. For the 1D PBR the rapid consumption of $O_2$ close to its inlet is visible. The conversion of $CH_4$ similarly takes place early in the reactor and assumes its maximum value at the point where $O_2$ depletes, following which the reactor's performance remains unchanged. 2D MR simulation results at equivalent conditions show that a much larger catalytic bed length is required to attain a similar $CH_4$ conversion to that of the PBR (Figure 2). Clearly at these conditions $CH_4$ consumption in the MR is controlled by the availability of $O_2$, the former progressively permeating through the membrane. For both reactors $C_2$ selectivity is at its highest value close to the inlet, decreasing rapidly for the PBR and gradually for the MR along the reactor length. More importantly though, in the PBR with GM-2 a low $C_2$ yield of 8.28 % is obtained based on a 29.86 % $C_2$ selectivity at a 27.72 % $CH_4$ conversion, while in the MR a higher value of 11.63 % is achieved at a 47.86 % $C_2$ selectivity and 24.31 % $CH_4$ conversion. The higher amount of $O_2$ in the feed mixture of the PBR obviously promotes the deep oxidation of $CH_4$, but also of $C_2$ species produced via coupling. In the MR the gradual dosing of $O_2$ maintains a higher $CH_4/O_2$ ratio along the entire reactor length, which, given the higher order of selective reaction rates over unselective ones in terms of $CH_4$, promotes effectively the production of $C_2$ over $CO_x$.

Nonetheless, the incomplete conversion of $O_2$ in the 2D MR results needs also to be noted, with a value of 82.91 % at these conditions versus 100 % in the 1D PBR for a similar $CH_4$ conversion. 2D simulation results at these conditions presented in Figure 3 show that in the PBR, where reactants are co-fed, radial concentration variations are negligible for both reactants and products, justifying also the use of the 1D results in the analysis above. In the MR, though, the consumption of $O_2$ clearly takes place mostly close to the membrane, where

it permeates from in the tube, giving rise to strong radial concentration gradients for all species. The slower radial mass transport by diffusion results in $O_2$ that permeates but remains unutilized, impacting also on the conversion of $CH_4$. $C_2$ products are similarly formed closer to the boundary where most of the $O_2$ exists, slowly diffusing to the center. This uneven distribution results in a substantial loss of $C_2$ selectivity in the 2D model, since the $CH_4/O_2$ ratio close to the membrane wall, where most of the conversion takes place, is higher than at the center of the reactor. This can be also clearly seen if a 1D model is assumed for the MR. Table S4 shows that for the case of the GM-2 and $JO_2$-1 1D MR, both $CH_4$ and $O_2$ conversions can increase to 36.78 % and 96.57 %, respectively, with $C_2$ selectivity and yield similarly displaying a large rise to 53.76 % and 19.77 %, respectively. This is a clearly substantial increase in performance that could be achieved if radial concentration gradients could be minimized in the MR.

Comparison of the results obtained with the other considered gas phase networks in Table S4 further highlights the importance of correctly describing the OCM homogeneous chemistry. Substituting GM-2 with the less rigorous GM-1 model in both the 1D PBR and 2D MR leads to a sharp increase in $C_2$ selectivity from 29.86 % to 49.67 % and from 47.86 % to 64.79 %, respectively, leading to equivalent $C_2$ yield increases from 8.28 % to 15.58 % and from 11.63 % to 16.24 %, respectively. Results again indicate, as discussed in Section 2.4, that the GM-2 network describes unselective homogeneous pathways, not accounted for in GM-1. Additionally, results highlight that significant performance benefits exist and can be attained if these unselective gas phase pathways are avoided.

### 3.2 Comparison between MR and VTMR

As evidenced in section 3.1, distributed feeding of $O_2$ in membrane reactors can theoretically lead to higher $C_2$ selectivities and yields in comparison to co-feed packed bed reactors, however radial concentration gradients can decrease significantly this benefit. A smaller reactor

diameter can potentially reduce the impact of radial dispersion, however the effect of secondary oxidation of products close to the membrane wall, especially towards the end of the reactor, needs to be addressed differently. As described in Section 2, a variable thickness membrane reactor (VTMR) is proposed in this work, with its specifications optimized aiming at maximizing the selectivity towards $C_2$ species. Final optimal values for the thickness of the membrane at axial position $z = 0$ and the slope of its increase for each case considered are presented in Table 4, while Table 3 summarizes again the equivalent performance metrics in line with results presented in previous sections.

Figure 4 compares the permeation flux across the membrane with the net rate of consumption of $O_2$ along the reactor's length for the 2D MR and VTMR using GM-2 and $JO_2$-1. In the 2D MR the permeation flux remains almost constant across the reactor's length, since, as soon as $O_2$ starts permeating, a stable $O_2$ partial pressure gradient exists with the shell side close to the boundary of the constant thickness membrane. The net rate of $O_2$ consumption, though, which is calculated across the radius of the reactor, is at zero value at the inlet of the reactor and rises quickly once $O_2$ starts permeating. As evident from Figure 4 the flux and consumption rates never become equal in the 2D MR due to the unutilised $O_2$ that does reach the center of the reactor. In the 2D VTMR though a gradual decrease along the length of the reactor in the permeation flux is observed due to the increasing thickness of the membrane, while the parameter has values always below those predicted for the MR. The consumption rate of $O_2$ in the VTMR again initially is at a value of zero but becomes very quickly almost equal to the permeation flux.

Overall, a significant increase in $C_2$ selectivity from 47.86 % to 67.26 % is achieved in the optimized VTMR, although at the expense of a decrease in $CH_4$ conversion from 24.31 % to 16.73 %, resulting in equivalent $C_2$ yields for the two reactors at approximately 11.5 % (Table 3). The decreasing $O_2$ flux in the VTMR leads to a higher $CH_4/O_2$ ratio across the entire reactor

length in comparison to the MR that enhances selectivity, originating, primarily, from a decreased rate of unselective reactions and, secondly, from a relative promotion of the selective oxidative coupling of methane. From Table 3 it can further be seen that in the VTMR the conversion of $O_2$ increases from 82.91 % to 91.25 %, consistent with the aforementioned almost equal consumption rate and permeation flux of $O_2$ shown in Figure 4. The results demonstrate the higher utilization degree of the permeating $O_2$ in the VTMR, further indicating that $CH_4$ conversion in the MR is clearly limited by radial diffusion, while in the VTMR it is mainly driven by the availability of $O_2$, so diffusional limitations would be easier to overcome via the optimization of the reactor design. Qualitatively similar results were obtained for all cases studied (Table S4 in SI), so these are not further discussed here.

The gain in performance in terms of $C_2$ selectivity is further demonstrated in presenting the $CH_4$ and $C_2$ concentration profiles in both reactors for the 2D case (Figure 5). Ethylene and ethane are in both cases produced primarily close to the membrane, diffusing to the center of the reactor, however clearly the VTMR concentration profiles are higher for both species. The difference is particularly visible for $C_2H_6$, consistent with it being a primary product in the kinetic mechanism of OCM, but is also visible for $C_2H_4$, whose formation as a secondary product is enhanced towards the latter half of the reactor.

Current results indicate that the VTMR concept is preferable to the MR in obtaining a similar $C_2$ yield, but at a higher selectivity, rather than for achieving an overall higher yield. The comparative gain in $C_2$ selectivity at the expense of $CH_4$ conversion is further evidenced in Figure 6, which presents the effect of space time (varied by changing the total volumetric flow rate) on the performance of the VTMR in comparison to the MR for the 2D case using GM-2 and $JO_2$-1. Across the entire range investigated the VTMR performs substantially better in terms of $C_2$ selectivity, whereas $CH_4$ conversion is consistently lower than that of the MR. Similar findings have been reported in experimental investigations over porous ceramic

membranes [6,42]. Nonetheless, the increase of space time still leads to a gradual selectivity loss, with $C_2$ species eventually oxidized to $CO_x$ via a combined contribution of the gas phase radical and heterogeneous catalytic networks at the higher contact times studied. Particularly the production of vinyl radicals in the gas phase from ethylene via multiple radical reactions was found critical in relation to selectivity loss, indicating again the necessity of treating rigorously the OCM homogeneous chemistry. Even so, the gain on $C_2$ selectivity versus the impact on $CH_4$ conversion is favourable at practically all space times with the $C_2$ yield achieved being consistently higher to the equivalent one of the MR. It should also be noted that a lower $CH_4$ conversion indeed probably implies larger recycle streams [43], however the decrease in unselective products in the reactor outlet would represent a comparative advantage of the VTMR over the MR in terms of downstream separation needs. Lastly, it bears attention that the results in Figure 6 were obtained by only manipulating the total flow rate to achieve different space times, so without optimizing the configuration of the VTMR at each point separately. It is expected that following such an optimization, further performance improvements could be achieved.

Finally, given the findings above and to allow for a fairer evaluation of the VTMR concept, a further comparison of the MR and VTMR configuration was pursued at a similar $CH_4$ conversion. To achieve the latter the simulated length of the VTMR was increased, keeping all other configuration details fixed, so that a conversion of $CH_4$ equal to that of the MR case was obtained. Results compared to those obtained with the MR at a space time of 7.85 s for the 2D cases using $JO_2$-1 and GM-1 are shown in the bottom rows of Table 3, while in Table S4 in the SI the same results are presented for all reaction networks and reactor models studied. For all the cases evaluated the VTMR shows a higher $C_2$ selectivity and, as such, $C_2$ yield, but, as expected, at the expense of a longer reactor length. Indicatively, for the 2D case extending the VTMR's length to achieve the same conversion as in the MR, leads to a 20 % increase in the

achieved $C_2$ yield. Hence, the benefits of the VTMR in terms of $C_2$ selectivity are indeed maintained also at conversion levels equivalent to those of the MR, underlining clearly the potential of the reactor concept.

### 3.3 Non-isothermal performance

The performance of the proposed VTMR is further investigated under adiabatic conditions and compared to that of the conventional MR (Figure 7). In both reactors, a temperature rise is observed close to their inlet, linked with the initiation of oxidative reactions, induced by the permeation of $O_2$ from the shell to the tube. Once $O_2$ starts permeating across the membrane, though, its concentration immediately rises above zero in the tube, affecting the chemical potential difference, leading to the suddenly decreasing $O_2$ flux in both reactors. After that stage though, the rising temperature in the tube enhances the permeation flux across the membrane (according to equation (10)). Nonetheless, the axial temperature profile in the VTMR increases clearly less rapidly in comparison to the MR. In the MR, the temperature displays a continuous rise, as the constantly permeating $O_2$ accelerates exothermic reactions, which in turn enhance the flux through the membrane due to the rising temperature. In the VTMR, though, the increasing thickness of the membrane manages to avoid the rise in the $O_2$ permeation flux, which in turn results in relatively constant $O_2$ consumption rates, achieving a much smoother axial temperature profile (Figure 7). Clearly, the likelihood of hotspot generation or runaway reactions taking place in the VTMR is significantly reduced through the modulation of $O_2$ permeation. Equivalent observations were reported in studies of similar reactor concepts for the autothermal reforming of methane [21] and the selective oxidation of o-xylene to phthalic anhydride [2]. A maximum temperature difference of about 200 K is observed between the two configurations for the simulated conditions at the end of the reactor. Radial gradients are also milder in the VTMR versus the MR, with temperature differences

reaching more than 100 K in the MR, while in the VTMR these never surpass 40 K, indicative of the discussed process safety benefits.

The modulation of $O_2$ flux in the VTMR, already elaborated previously, in combination with the more efficient temperature control described above lead to an overall performance enhancement in comparison to the MR. Table 5 summarizes results on both reactors at adiabatic conditions using the $JO_2$-1 and GM-2 models for the 2D case at a space time of 1.57 s, while equivalent results obtained with the 1D models are provided in Table S5 in the SI. As in Section 3.2, to obtain a fair comparison, the performance of the two reactors at both equal lengths and positions of similar conversion is considered. Consistent with the findings during isothermal simulations, for equal lengths (0.1 m) the VTMR achieves a substantially higher $C_2$ selectivity (59.76 % versus 30.90 %) at lower $CH_4$ conversion (10.55 % versus 16.91 %) than the MR, resulting in a higher $C_2$ yield of 6.30 % versus 5.23 %. To attain the same $CH_4$ conversion with the MR, a longer VTMR is required (e.g. 0.24 m versus 0.10 m for ~16 % conversion or 0.1 m versus 0.05 m for ~10.5 % conversion). At all cases though, the achieved $C_2$ selectivity at these "iso-conversion" reactor lengths is always higher in the VTMR resulting in a higher $C_2$ yield. For example, at lengths 0.24-0.10 m a favourable $C_2$ selectivity of 46.07 % for VTMR versus 30.90 % for MR is achieved, leading to a $C_2$ yield of 7.70 % over 5.23 %. Furthermore, as seen in Table S5 in the SI, when equivalent lengths are considered with 1D models, a better performance is predicted in comparison to the 2D VTMR for $C_2$ selectivity (76.71 % versus 59.76 %) at approximately equivalent $CH_4$ conversion. These results highlight again the need for reactor design to target the minimisation of radial gradients, in line with discussions in the previous sections.

Indicatively, simulation results with a co-feed adiabatic 2D PBR model at equivalent conditions were also conducted, displaying a significantly higher $CH_4$ conversion of 44.15 %, however at severely decreased $C_2$ selectivity of only 13.09 %. Furthermore, a very strong exotherm takes

place close to the reactor's entrance, given the concurrent feeding of reactants, which would pose serious materials stability, safety and control issues in the real application (Figure 7). The benefits achieved by the distributed and modulated $O_2$ feeding in membrane reactors are clearly evident from their $O_2$ consumption rate profiles shown in Figure 7, which follow closely the equivalent $O_2$ permeation fluxes, avoiding as such uncontrolled oxidation. Especially, for the VTMR the modulated $O_2$ permeation led to an optimal heat release and reaction rates profile towards selective products.

### 3.4 Discrimination between $O_2$ surface exchange reactions and diffusion

The significance of the surface exchange kinetics of $O_2$ at the membrane interfaces versus its bulk diffusion across the membrane has been identified in different studies [14,36,44]. Both processes affect the rate of $O_2$ permeation across the membrane, with bulk diffusion being dominant in thick membranes and surface kinetics becoming rate limiting as membrane thickness decreases. Nonetheless, no reports have addressed the quantification of the respective contribution of these processes for a varying thickness membrane used for the OCM process. Figure 8 shows the $O_2$ permeation fluxes predicted for the 1D VTMR using the more rigorous $JO_2$-2 model, as well as the predictions of this model when each of the three resistances has been considered as limiting (see Section 2.3 and equation (11) for details). Results for three membrane configurations of different initial thickness, but of constant slope of thickness increase, are presented. Clearly, for all cases considered the resistances due to bulk diffusion and surface reactions on the tube side are much more significant than that of surface reactions on the shell side. Moreover, as expected, it can be seen that the rate of $O_2$ diffusion across the membrane increases as the membrane thickness decreases. This leads to the overall $O_2$ permeation flux being affected by both the surface exchange kinetics on the tube side and the rate of diffusion of $O_2$ across the membrane at varying degrees dependent on the membrane thickness. For an initial thickness of 0.003 m and 0.00076 m, the overall $O_2$ permeation flux is

predominantly controlled by diffusion. However, at an initial thickness of 0.0002 m the limitation by tube-side surface kinetics becomes pronounced, since the rate of diffusion of $O_2$ across the very thin membrane has increased significantly, in line with results reported in [39].

In Figure 8 the predictions of the $JO_2$-1 model are also provided for comparison at the same conditions. Only for this section the $JO_2$-1 expression is parameterized based on the values of Tsai et al. [35] for $Sr_{0.6}$, since the $JO_2$-2 model was also developed on a LSCF membrane. It is interesting to note that both $JO_2$-1 and $JO_2$-2 are in relatively good agreement with each other at the cases of initial membrane thicknesses of 0.003 m and 0.0076 m, where diffusion limitations are dominant, indicating that $JO_2$-1 is sufficient for such cases. At 0.0002 m where surface kinetics become limiting though, the deviation in the predictions of the two models become obvious. The constantly higher flux predicted by $JO_2$-1 in this case of a very thin membrane results actually in such a high $O_2$ permeation flux that leads to the depletion of the latter in the shell side and is the reason for the sharp drop displayed in flux profile at the middle of the reactor. However, the $JO_2$-2 predictions indicate that this is not a realistic evolution of the profile, as tube-side surface exchange kinetics would be limiting the flux in this case.

The transition from diffusion control to surface exchange control depends also on the temperature [39]. Figure 9 presents the effect of temperature on the permeation flux predicted by $JO_2$-2 and its individual components at two different membrane thicknesses. Here constant thickness MR simulation results are presented, so as to be able to probe the effect of temperature independently of the thickness of the membrane. It is evident that as temperature increases the surface exchange rates increase faster than the diffusion rate, consistent with their approximately three times greater activation energy in comparison to the diffusion one (see Table S1 and S2 in SI). Furthermore, the temperature influence on the overall flux is clearly more pronounced in the case of the thinner membrane studied (0.0002 m), since the thicker one of 0.003 m is diffusion limited across the entire temperature range. For the thinner membrane,

the overall $O_2$ permeation flux at 973 K is predominantly limited by surface exchange kinetics on the tube side and as temperature increases to 1103 K the influence of $O_2$ diffusion becomes more important, with 1020 K being approximately the transition point after which both mechanisms are contributing significantly. To summarize, the consideration of both diffusion and surface exchange kinetics limitations on the total $O_2$ flux appears necessary for particularly thin dense membranes, such as those supported on porous layers e.g. in asymmetric configurations [10,45].

## 4 Conclusions

The VTMR concept investigated in the current work was shown to be able to lead to important $C_2$ selectivity improvements for the OCM process. The gradual decrease in the $O_2$ permeation flux across the length of the reactor allows for the secondary oxidation of $C_2$ products to be minimized. Moreover, the concept provides a much better control of temperature within the reactor, reducing the possibility of hotspot generation, benefiting safety and catalyst stability and reactor materials requirements. The above advantages were found to be possible in the VTMR at the expense of reduced $CH_4$ conversion in comparison to conventional membrane reactors, given the reduced $O_2$ that permeates on account of the increasing membrane thickness, however not impacting the overall $C_2$ yield achieved. Increasing the reactor length of the VTMR allows reaching similar conversion levels to conventional membrane reactors, but at higher $C_2$ selectivity, hence also $C_2$ yield. Homogeneous gas phase reactions and radial diffusion limitations were found to be main $C_2$ selectivity loss factors in all reactor configurations studied. The use of a variable thickness membrane led to enhanced performance by utilizing $O_2$ optimally towards selective pathways, however future developments should further address the impact of radial gradients and homogeneous reactions within the VTMR concept. Thin dense membranes supported on porous layers would appear to be a promising method to implement the VTMR configuration, where it has been demonstrated that in certain

cases surface exchange kinetics would be limiting the permeation flux. Through the analysis conducted, the potential of using variable thickness membranes for OCM, as conceptualized in the current study, was clearly demonstrated.

# Nomenclature

A: pre-exponential factor, mol $m^{-1}$ $s^{-1}$ $K^{-1}$

$C_i$: concentration of component $i$, mol $m^{-3}$

$C_{pi}$: specific heat capacity of component $i$, kJ $mol^{-1}$ K

$d_t$: tube diameter, m

$d_m$: log mean tube diameter, m

$d_p$: catalyst diameter, m

$D_{er}$: effective bulk diffusivity of gas mixture, $m^2$ $s^{-1}$

$D_v$: oxygen vacancy bulk diffusion coefficient, $m^2$ $s^{-1}$

$E_a$: activation energy, kJ $mol^{-1}$

$F_i$: molar flow of species $i$, mol $s^{-1}$

$J_i$: permeation flux of species $i, where\ i = O_2$, mol $m^{-2}$ $s^{-1}$

$k_f$: forward surface exchange rate constant, $m.atm^{-0.5}.s^{-1}$

$k_r$: reversed surface exchange rate constant, $mol.m^{-2}.s^{-1}$

$L_m$: membrane thickness, m

$L_z$: reactor length, m

$P_{O_{2,t}}$: partial pressure of $O_2$ in the tube, kPa

$P_{O_{2,s}}$: partial pressure of $O_2$ in the shell, kPa

$r$: radial position, m

$R$: gas constant, 8.314 J $mol^{-1}$ $K^{-1}$

$R_j$: rate of reaction $j$, mol $m^{-3}$ $s^{-1}$

$T$: temperature, K

$U_a$: overall heat transfer coefficient through the membrane tube wall, W $m^{-2}$ $K^{-1}$

$U_z$: linear velocity, m $s^{-1}$

$z$: axial direction, m

**Greek Letters**

$\alpha_w$: membrane wall heat transfer coefficient, W $m^{-2}$ $K^{-1}$

$\beta$: vector of independent variables (-)

$\Delta H_{R_j}$: reaction enthalpy, kJ $mol^{-1}$

ε: catalyst bed porosity, $m_g^3\ m_r^{-3}$, (-)

$\lambda_{er}$: effective radial thermal conductivity, W $m^{-1}$ $K^{-1}$

$\rho$: density of catalyst, kg $m^{-3}$

$\sigma$: slope of linear equation (-)

**Subscripts**

avg: average between the shell and tube sides (refers to temperature)

er: effective radial

g: gas phase

r: reactor

t: tube

s: shell

m: membrane

w: wall

z: axial position

$i$: number of components

$j$: number of reactions

0: initial value

# References


[1] M. Eramo, Global Ethylene Market Outlook, (2017).

[2] S.M. Aworinde, A.M. Schweidtmann, A.A. Lapkin, The concept of selectivity control by simultaneous distribution of the oxygen feed and wall temperature in a microstructured reactor, Chem. Eng. J. 331 (2018) 765–776.

[3] G.E. Keller, M.M. Bhasin, Synthesis of ethylene via oxidative coupling of methane. I. Determination of active catalysts, J. Catal. 73 (1982) 9–19.

[4] A. Galadima, O. Muraza, Revisiting the oxidative coupling of methane to ethylene in the golden period of shale gas: A review, J. Ind. Eng. Chem. 37 (2016) 1–13.

[5] C. Karakaya, H. Zhu, C. Loebick, J.G. Weissman, R.J. Kee, A detailed reaction mechanism for oxidative coupling of methane over $Mn/Na_2WO_4/SiO_2$ catalyst for non-isothermal conditions, Catal. Today. 312 (2018) 10–22.

[6] H.R. Godini, A. Gili, O. Görke, U. Simon, K. Hou, G. Wozny, Performance analysis of a porous packed bed membrane reactor for oxidative coupling of methane: Structural and operational characteristics, Energy and Fuels. 28 (2014) 877–890.

[7] B.L. Farrell, V.O. Igenegbai, S. Linic, A viewpoint on direct methane conversion to ethane and ethylene using oxidative coupling on solid catalysts, ACS Catal. 6 (2016) 4340–4346.

[8] K. Otsuka, S. Yokoyama, A. Morikawa, Catalytic activity-and selectivity-control for oxidative coupling of methane by oxygen-pumping through yttria-stabilized zirconia, Chem. Lett. 14 (1985) 319–322.

[9] L. Olivier, S. Haag, C. Mirodatos, A.C. van Veen, Oxidative coupling of methane using catalyst modified dense perovskite membrane reactors, Sel. Pap. Present. Sess. 10, Nat. Gas Conversion, Eur. VIII Conf. Turku (Åbo), Finland, August 26-31, 2007. 142 (2009) 34–41.

[10] N.H. Othman, Z. Wu, K. Li, An oxygen permeable membrane microreactor with an in-situ deposited $Bi_{1.5}Y_{0.3}Sm_{0.2}O_{3-\delta}$ catalyst for oxidative coupling of methane, J. Memb. Sci. 488 (2015) 182–193.

[11] W. Wang, Y.S. Lin, Analysis of oxidative coupling of methane in dense oxide membrane reactors, J. Memb. Sci. 103 (1995) 219–233.

[12] S.J. Xu, W.J. Thomson, Perovskite-type oxide membranes for the oxidative coupling of methane, AIChE J. 43 (1997) 2731–2740.

[13] S. Smart, S. Liu, J.M. Serra, A. Basile, J.C. Diniz da Costa, 7 - Perovskite membrane reactors: fundamentals and applications for oxygen production, syngas production and hydrogen processing, in: A. Gugliuzza, A. Basile (Eds.), Membr. Clean Renew. Power Appl., Woodhead Publishing, 2014: pp. 182–217.

[14] X. Zhu, H. Liu, Y. Cong, W. Yang, Permeation model and experimental investigation of mixed conducting membranes, AIChE J. 58 (2012) 1744–1754.

[15] Y.K. Kao, L. Lei, Y.S. Lin, Optimum operation of oxidative coupling of methane in porous ceramic membrane reactors, 5th Int. Conf. Catal. Membr. React. 82 (2003) 255–273.

[16] Y. Lu, A.G. Dixon, W.R. Moser, Y. Hua Ma, Oxidative coupling of methane in a modified γ-alumina membrane reactor, Chem. Eng. Sci. 55 (2000) 4901–4912.

[17] A.M. Ramachandra, Y. Lu, Y.H. Ma, W.R. Moser, A.G. Dixon, Oxidative coupling of methane in porous Vycor membrane reactors, J. Memb. Sci. 116 (1996) 253–264.

[18] S. Jaso, H. Arellano-Garcia, G. Wozny, A novel design concept for the oxidative coupling of methane using hybrid reactors, in: E.N. Pistikopoulos, M.C. Georgiadis, A.C. Kokossis (Eds.), 21st Eur. Symp. Comput. Aided Process Eng. - ESCAPE 21, Elsevier B.V., 2011: pp. 377–381.

[19] J. Hüppmeier, M. Baune, J. Thöming, Interactions between reaction kinetics in ATR-reactors and transport mechanisms in functional ceramic membranes: A simulation approach, Chem. Eng. J. 142 (2008) 225–238.

[20] J. Hüppmeier, S. Barg, M. Baune, D. Koch, G. Grathwohl, J. Thöming, Oxygen feed membranes in autothermal steam-reformers – A robust temperature control, Adv. Foss. Energy Util. 89 (2010) 1257–1264.

[21] M.A. Murmura, M. Diana, R. Spera, M.C. Annesini, Modeling of autothermal methane steam reforming: Comparison of reactor configurations, Chem. Eng. Process. Process Intensif. 109 (2016) 125–135.

[22] T.P. Tiemersma, C.S. Patil, M. van Sint Annaland, J.A.M. Kuipers, Modelling of packed bed membrane reactors for autothermal production of ultrapure hydrogen, Chem. Eng. Sci. 61 (2006) 1602–1616.

[23] Y.K. Kao, L. Lei, Y.S. Lin, A comparative simulation study on oxidative coupling of methane in fixed-bed and membrane reactors, Ind. Eng. Chem. Res. 36 (1997) 3583–3593.

[24] W. Kiatkittipong, T. Tagawa, S. Goto, S. Assabumrungrat, K. Silpasup, P. Praserthdam, Comparative study of oxidative coupling of methane modeling in various types of reactor, Chem. Eng. J. 115 (2005) 63–71.

[25] H.R. Godini, H. Arellano-Garcia, M. Omidkhah, R. Karimzadeh, G. Wozny, Model-based analysis of reactor feeding policies for methane oxidative coupling, Ind. Eng. Chem. Res. 49 (2010) 3544–3552.

[26] M. Daneshpayeh, A. Khodadadi, N. Mostoufi, Y. Mortazavi, R. Sotudeh-Gharebagh, A. Talebizadeh, Kinetic modeling of oxidative coupling of methane over $Mn/Na_2WO_4/SiO_2$ catalyst, Fuel Process. Technol. 90 (2009) 403–410.

[27] N. Holst, S. Jašo, H.R. Godini, S. Glöser, H. Arellano-Garcia, G. Wozny, J. Steinbach, Two-dimensional model for oxidative coupling of methane in a packed-bed membrane reactor, Chem. Eng. Technol. 35 (2012) 294–301.

[28] P.M. Couwenberg, Q. Chen, G.B. Marin, Irreducible mass-transport limitations during a heterogeneously catalyzed gas-phase chain reaction: Oxidative coupling of methane, Ind. Eng. Chem. Res. 35 (1996) 415–421.

[29] P.N. Kechagiopoulos, J.W. Thybaut, G.B. Marin, Oxidative coupling of methane: A microkinetic model accounting for intraparticle surface-intermediates concentration profiles, Ind. Eng. Chem. Res. 53 (2014) 1825–1840.

[30] D.E. Mears, On the relative importance of intraparticle and interphase transport effects in gas-solid catalysis, J. Catal. 30 (1973) 283–287.

[31] J.M.M. Smith, Chemical engineering kinetics, AIChE J. 2 (1956) 281–281.

[32] P.B. Weisz, Diffusion and chemical transformation, Science (80-. ). 179 (1973) 433–440.

[33] Z. Stansch, L. Mleczko, M. Baerns, Comprehensive kinetics of oxidative coupling of methane over the $La_2O_3/CaO$ catalyst, Ind. Eng. Chem. Res. 36 (1997) 2568–2579.

[34] Q. Chen, P.M. Couwenberg, G.B. Marin, The oxidative coupling of methane with cofeeding of ethane, Catal. Today. 21 (1994) 309–319.

[35] C.-Y. Tsai, A.G. Dixon, W.R. Moser, Y.H. Ma, Dense perovskite membrane reactors for partial oxidation of methane to syngas, AIChE J. 43 (1997) 2741–2750.

[36] S.J. Xu, W.J. Thomson, Oxygen permeation rates through ion-conducting perovskite membranes, Chem. Eng. Sci. 54 (1999) 3839–3850.

[37] X. Tan, K. Li, Design of mixed conducting ceramic membranes/reactors for the partial oxidation of methane to syngas, AIChE J. 55 (2009) 2675–2685.

[38] X. Tan, K. Li, Modeling of air separation in a LSCF hollow-fiber membrane module, AIChE J. 48 (2002) 1469–1477.

[39] S.J. Xu, W.J. Thomson, Perovskite-type oxide membranes for the oxidative coupling of methane, AIChE J. 43 (1997) 2731–2740.

[40] S. Dutta, Nontraditional Optimization, in: Optim. Chem. Eng., Cambridge University Press, 2016: pp. 222–257.

[41] F.G. Froment, B.K. Bischoff, Transport Processes with Fluid Solids Heterogeneous Reactions, 1st ed., John Wiley 8 Sons, New York Chichester Brisbane Toronto, 1979.

[42] J. Coronas, M. Menendez, J. Santamaria, Development of ceramic membrane reactors with a non-uniform permeation pattern. Application to methane oxidative coupling, Chem. Eng. Sci. 49 (1994) 4749–4757.

[43] J.W. Thybaut, G.B. Marin, C. Mirodatos, Y. Schuurman, A.C. van Veen, V.A. Sadykov, H. Pennemann, R. Bellinghausen, L. Mleczko, A novel technology for natural gas conversion by means of integrated oxidative coupling and dry reforming of methane, Chemie Ing. Tech. 86 (2014) 1855–1870.

[44] H.J.M. Bouwmeester, H. Kruidhof, A.J. Burggraaf, Importance of the surface exchange kinetics as rate limiting step in oxygen permeation through mixed-coducting oxides, Solid State Ionics. 72 (1994) 185–194.

[45] N.H. Othman, Z. Wu, K. Li, A micro-structured $La_{0.6}Sr_{0.4}Co_{0.2}Fe_{0.8}O_{3-\delta}$ hollow fibre membrane reactor for oxidative coupling of methane, J. Memb. Sci. 468 (2014) 31–41.

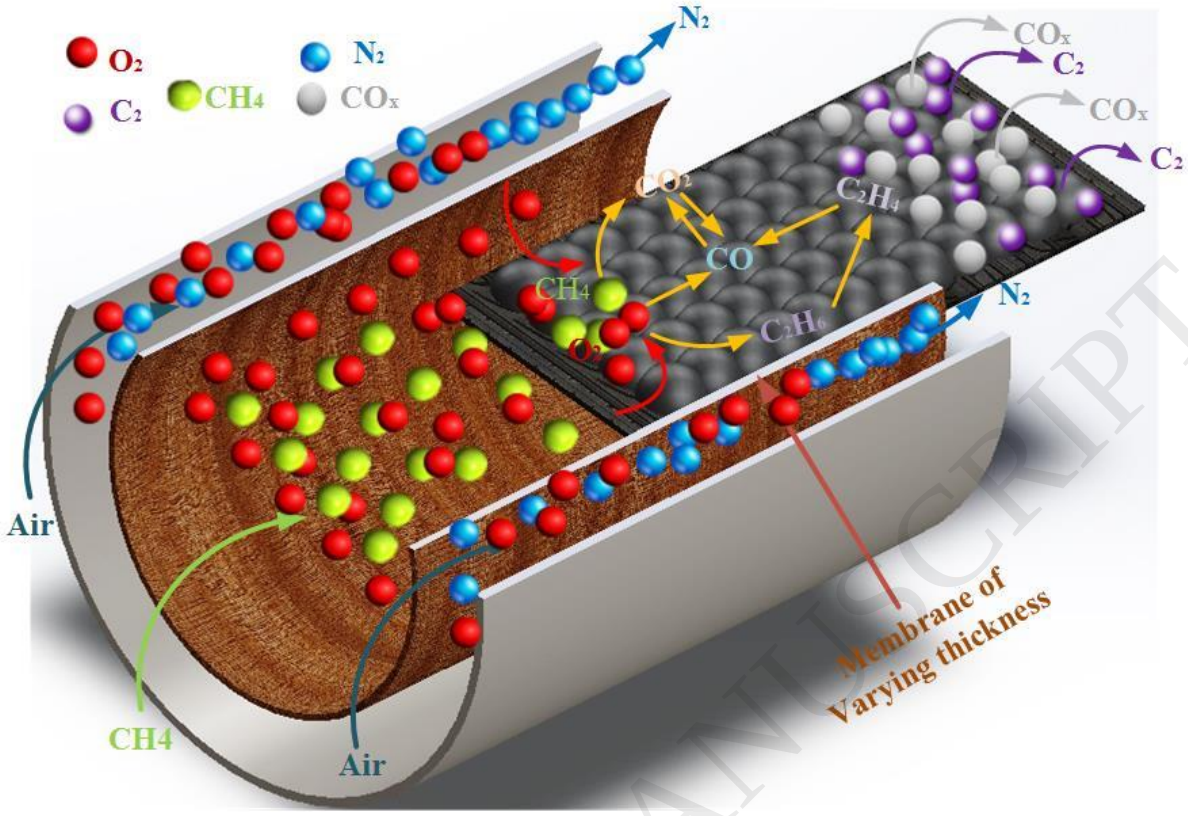


**Figure 1. VTMR conceptual reactor scheme and OCM reaction scheme. The same reactor configuration applies for MR except for the uniform membrane thickness, while in PBR, $O_2$, $CH_4$ and $N_2$ all enter the tube co-currently with no membrane being present. The reaction scheme highlights the main reaction pathways of carbon containing compounds according to** [33]**.**

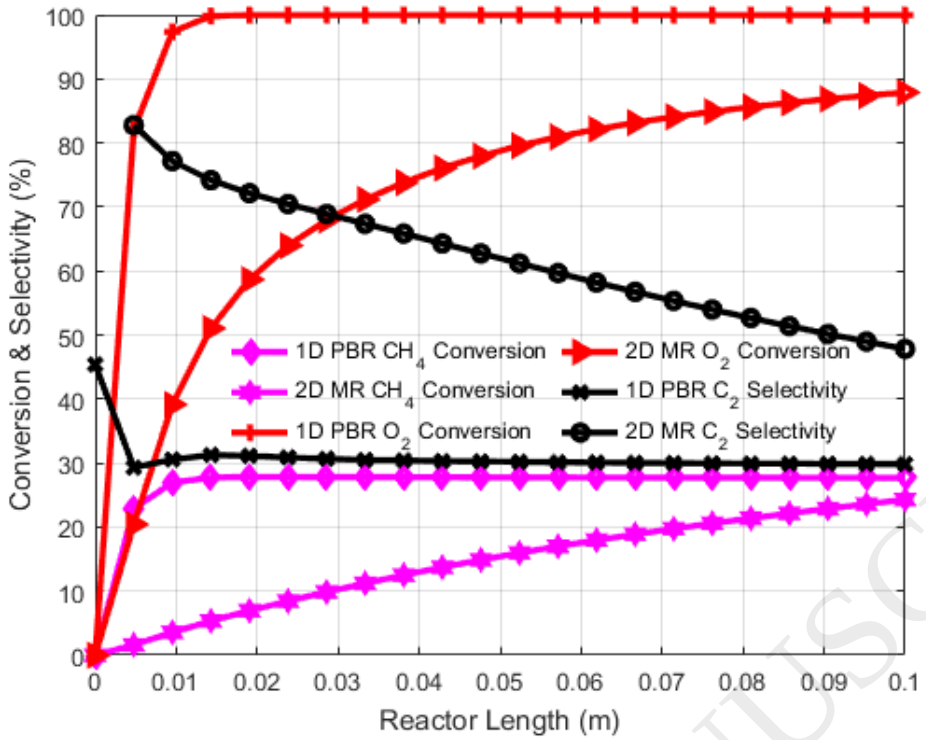


**Figure 2. Comparison of the performance of 1D PBR and 2D MR using GM-2 and $JO_2$-1. Inlet composition: Tube ($O_2$ = 0.0, $CH_4$ = 0.63, $N_2$ = 0.37) and Shell ($O_2$ = 0.21, $N_2$ = 0.79). Process conditions: Temperature = 1073 K, Pressure = 1 atm, $CH_4/O_2$ = 3.0 for PBR, $V_R/Q_{tot,0}$ = 7.85 s**

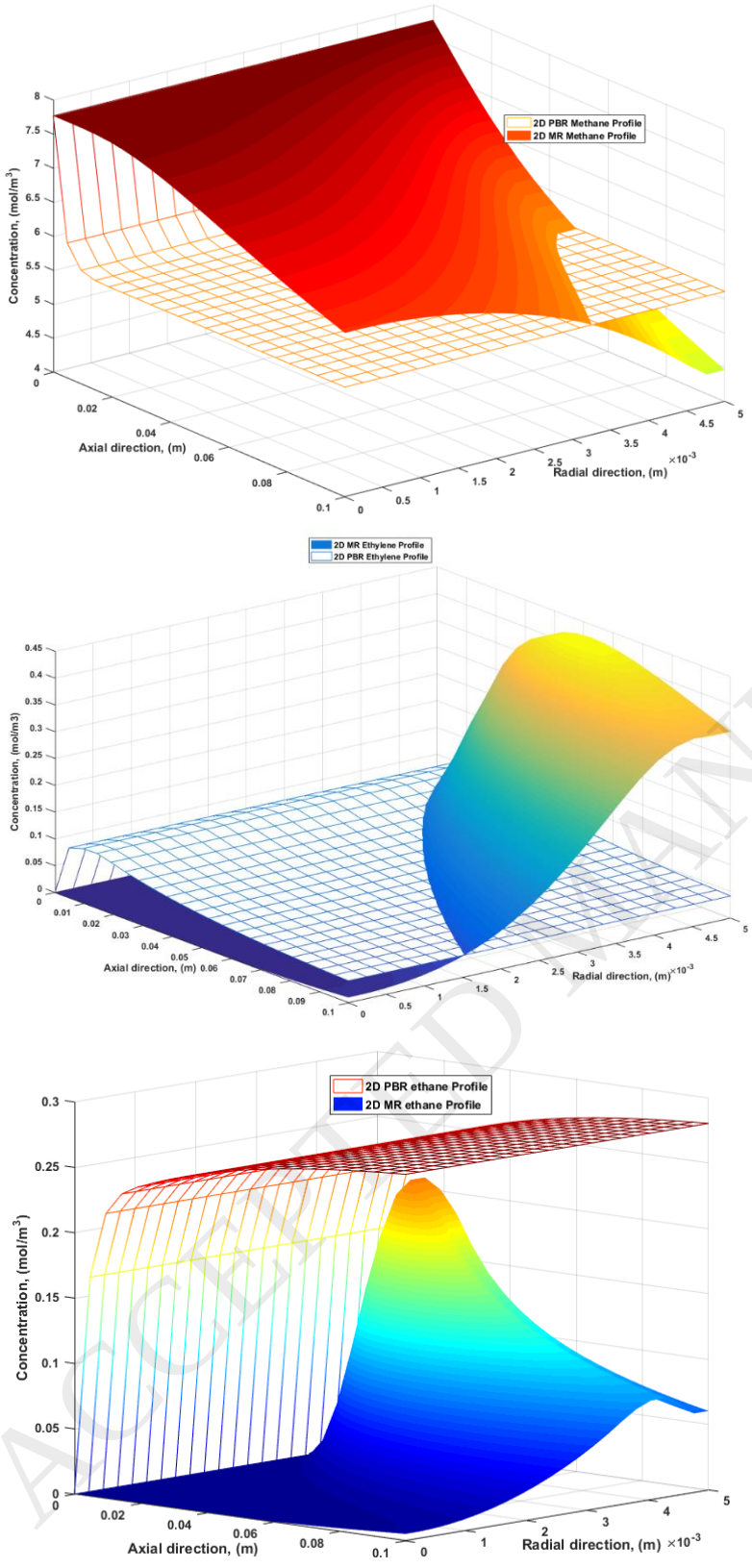


**Figure 3. Comparison of concentration profiles in the 2D PBR and MR using GM-2 and JO$_2$-1. Inlet composition: Tube ($O_2$ = 0.0, $CH_4$ = 0.63, $N_2$ = 0.37) and Shell ($O_2$ = 0.21, $N_2$ = 0.79). Process conditions: Temperature = 1073 K, Pressure = 1 atm, $CH_4/O_2$ = 3.0 for PBR, $V_R / Q_{tot,0}$ = 7.85 s.**

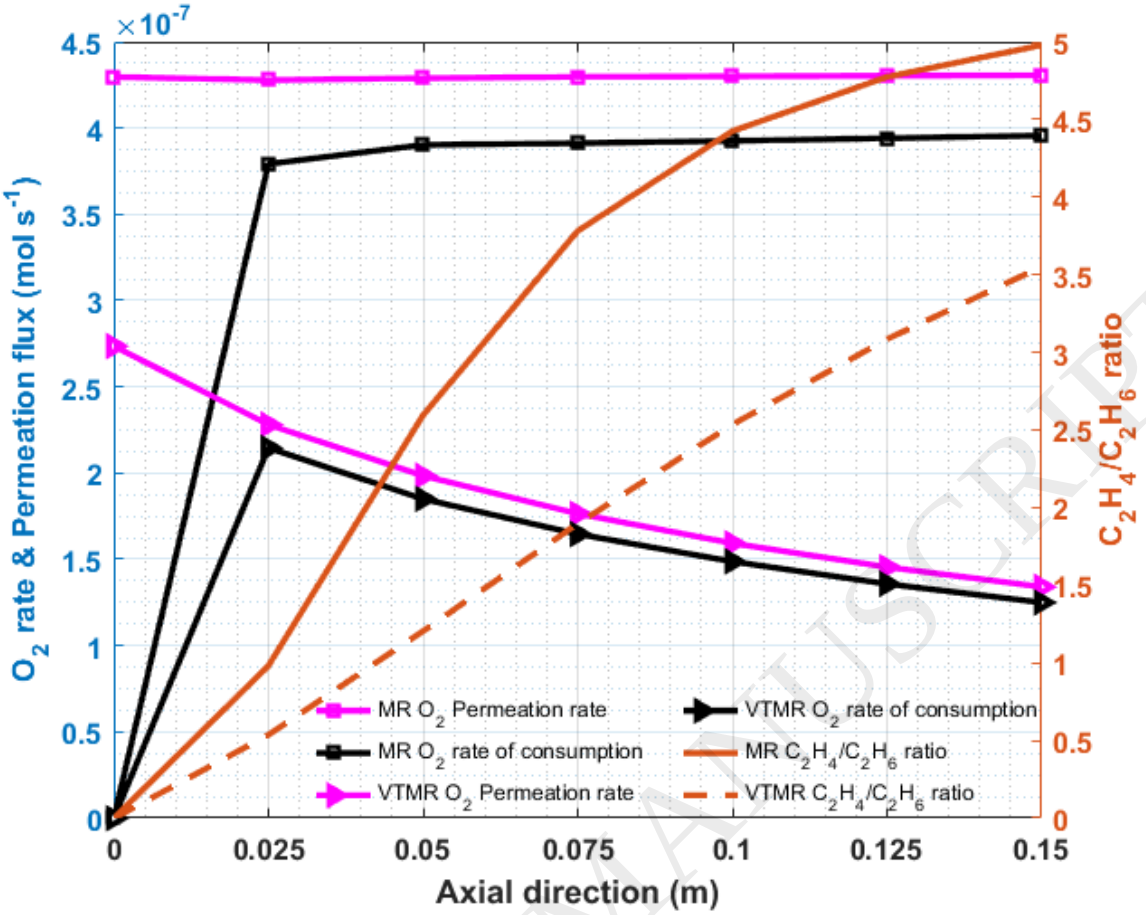


**Figure 4. Comparison of $O_2$ permeation flux and net rate of consumption in the 2D MR and VTMR using GM-2 and $JO_2$-1 (expressed in mol $s^{-1}$ through the multiplication with the respective membrane areas or reactor volumes of the differential elements along the axial direction over which they are calculated at). Inlet composition: Tube ($O_2$ = 0.0, $CH_4$ = 0.63, $N_2$ = 0.37) and Shell ($O_2$ = 0.21, $N_2$ = 0.79). Process conditions: Temperature = 1073 K, Pressure = 1 atm, $V_R/Q_{tot,0}$ = 7.85 s.**

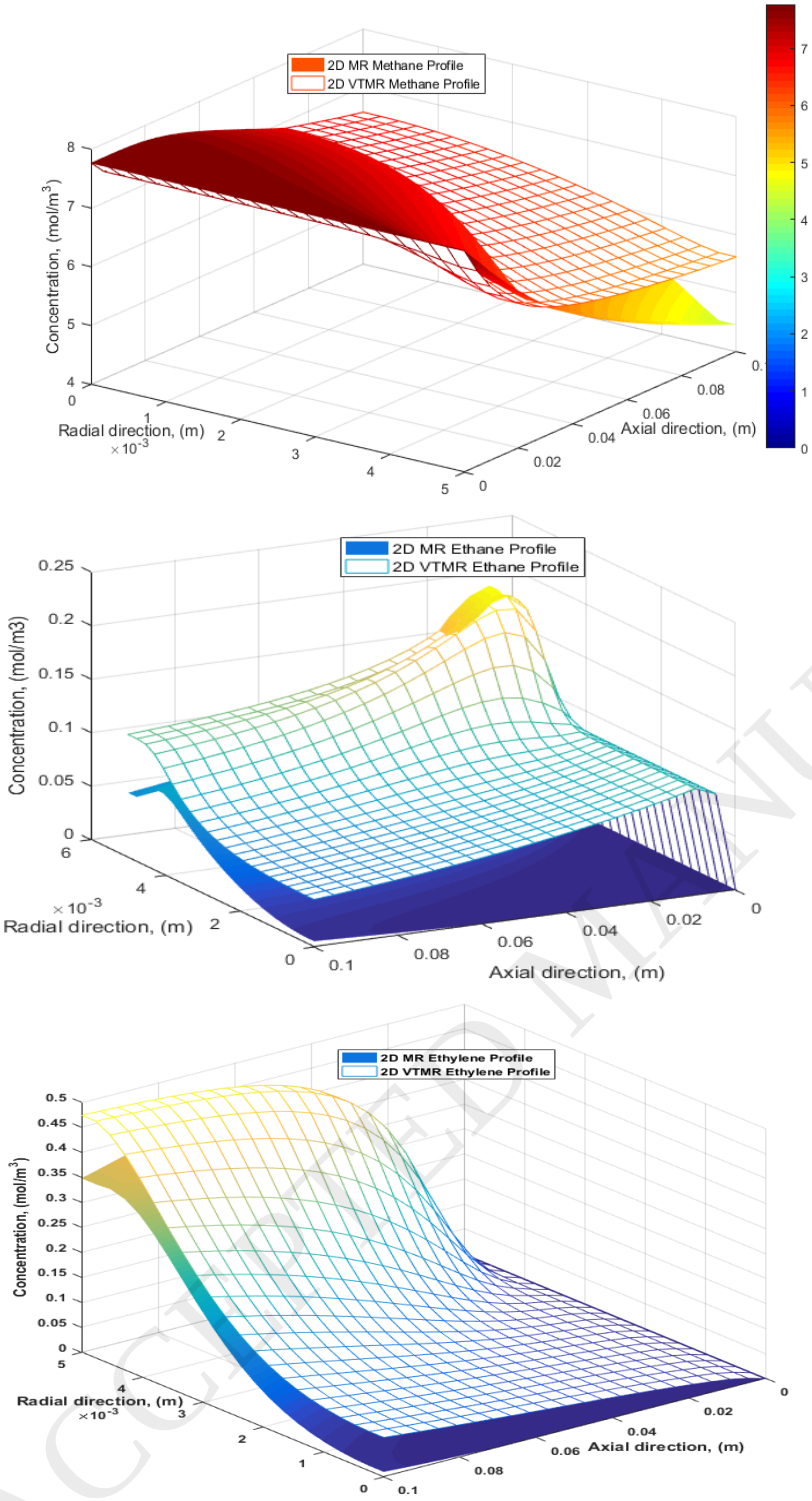


**Figure 5. Comparison of concentration profiles in the 2D MR and VTMR using GM-2 and JO$_2$-1. Inlet composition: Tube ($O_2$ = 0.0, $CH_4$ = 0.63, $N_2$ = 0.37) and Shell ($O_2$ = 0.21, $N_2$ = 0.79). Process conditions: Temperature = 1073 K, Pressure = 1 atm, $V_R/Q_{tot,0}$ = 7.85 s.**

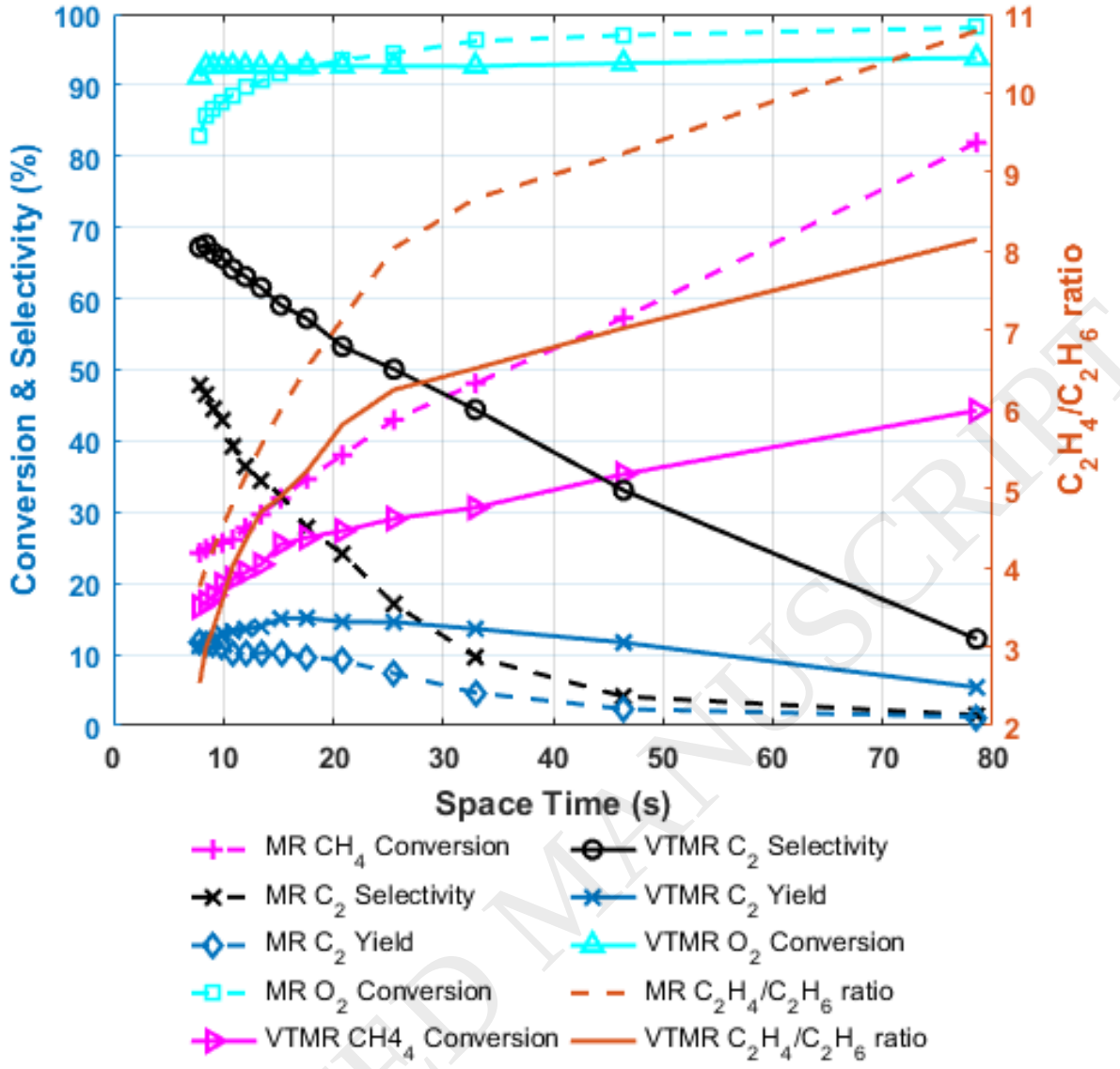


**Figure 6. Effect of space time ($V_R/Q_{tot,0}$) (via the manipulation of the total flow rate $Q_{tot,0}$) on the performance of the 2D MR and VTMR using GM-2 and JO2-1. Inlet composition: Tube ($O_2$ = 0.0, $CH_4$ = 0.63, $N_2$ = 0.37) and Shell ($O_2$ = 0.21, $N_2$ = 0.79). Process conditions: Temperature = 1073 K, Pressure = 1 atm.**

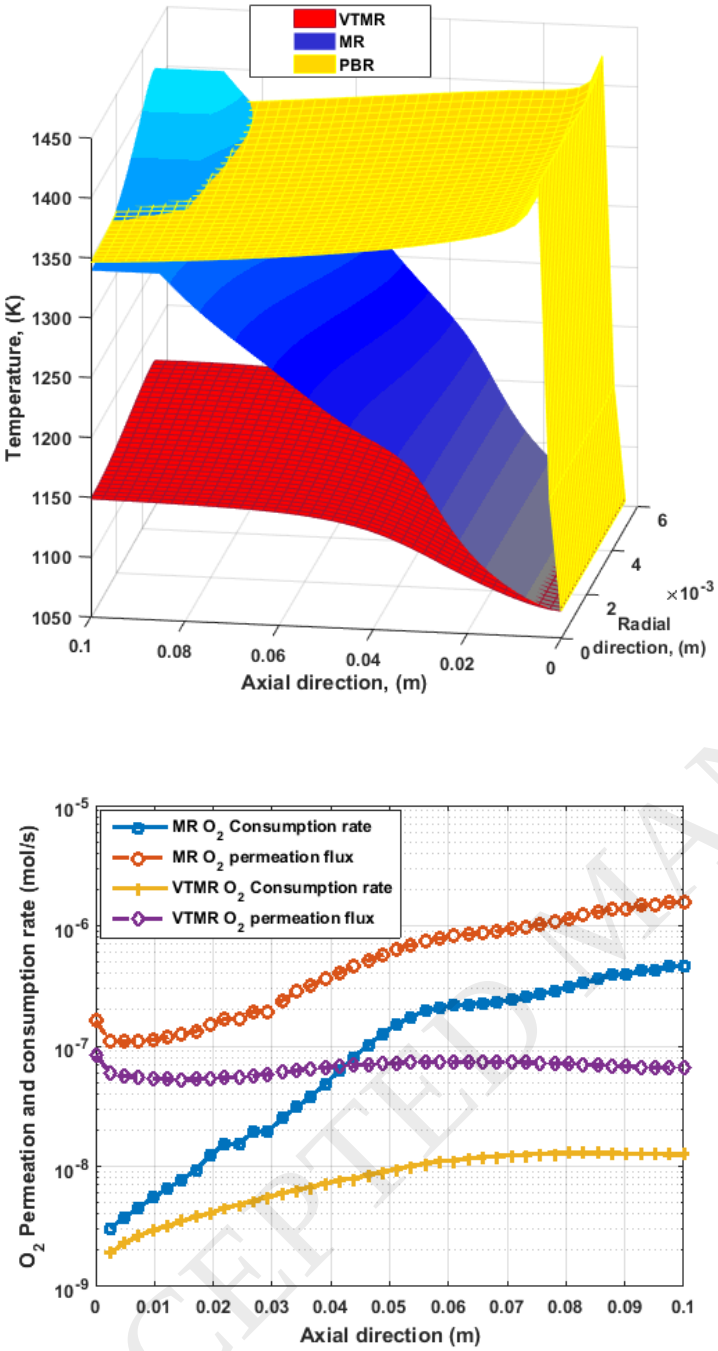


**Figure 7. Temperature [top] and $O_2$ permeation flux profiles [bottom] during adiabatic operation for the 2D PBR, MR and VTMR using GM-2 and $JO_2$-1 (flux expressed in mol $s^{-1}$ through the multiplication with the respective membrane area of the differential elements along the axial direction over which it is calculated at). Inlet composition: Tube ($O_2$ = 0.0, $CH_4$ = 0.63, $N_2$ = 0.37) and Shell ($O_2$ = 0.21, $N_2$ = 0.79). Process conditions: Temperature = 1073 K, Pressure = 1 atm, $V_R / Q_{tot,0}$ = 1.57 s.**

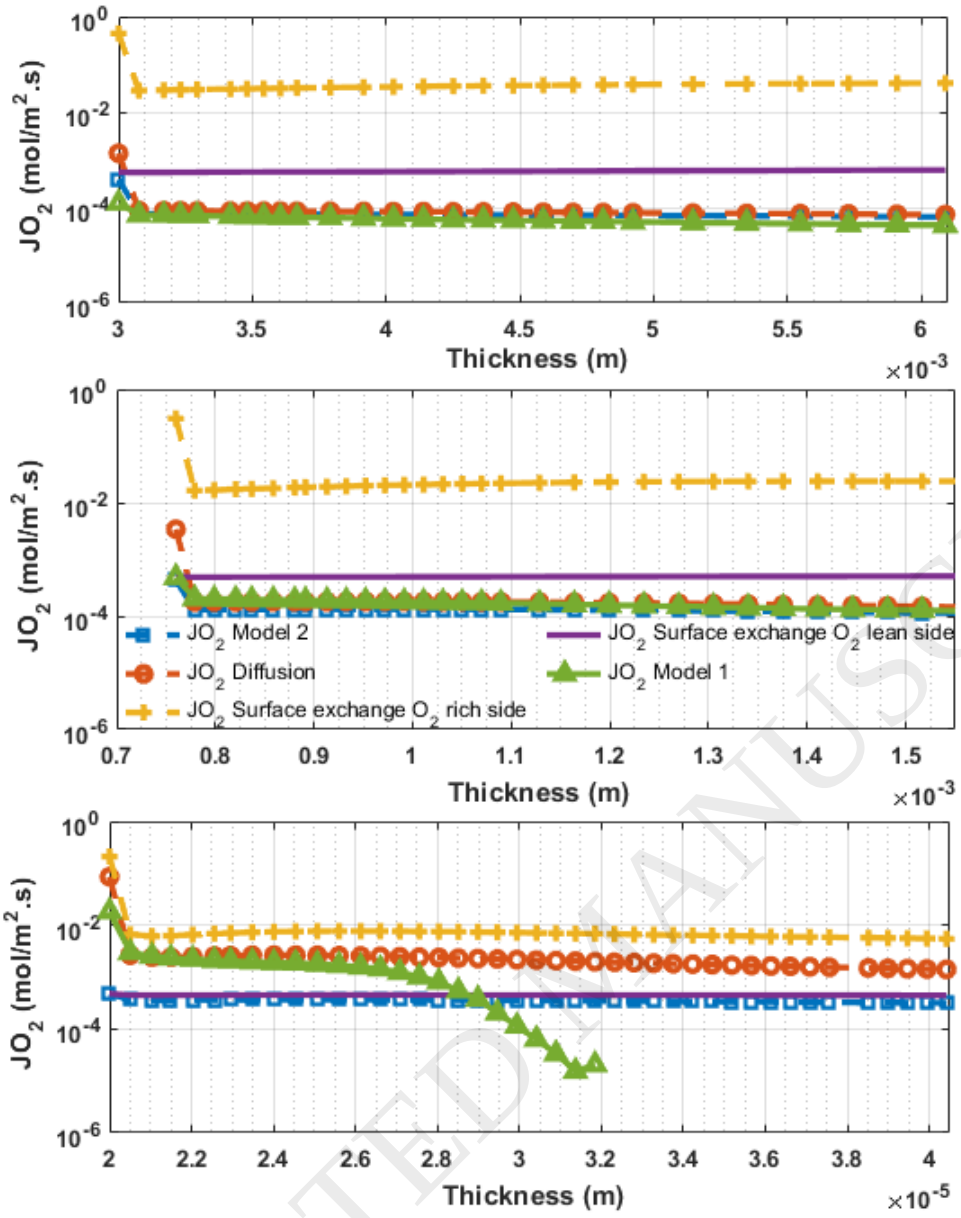


**Figure 8. Contribution of surface exchange kinetics and diffusion to the total rate of $O_2$ permeation across the membrane during 1D VTMR simulations using the full $JO_2$-2 flux model or only one of the three considered resistances as limiting. Predictions of $JO_2$-1 also shown for comparison. Initial membrane thickness: 0.003 m [Top], 0.00076 m [Middle], and 0.0002 m [Bottom]. Slope of thickness increase constant at 1.0. Inlet composition: Tube ($O_2$ = 0.0, $CH_4$ = 0.63, $N_2$ = 0.37) and Shell ($O_2$ = 0.21, $N_2$ = 0.79). Process conditions: Temperature = 1073 K, Pressure = 1 atm, $V_R/Q_{tot,0}$ = 7.85 s.**

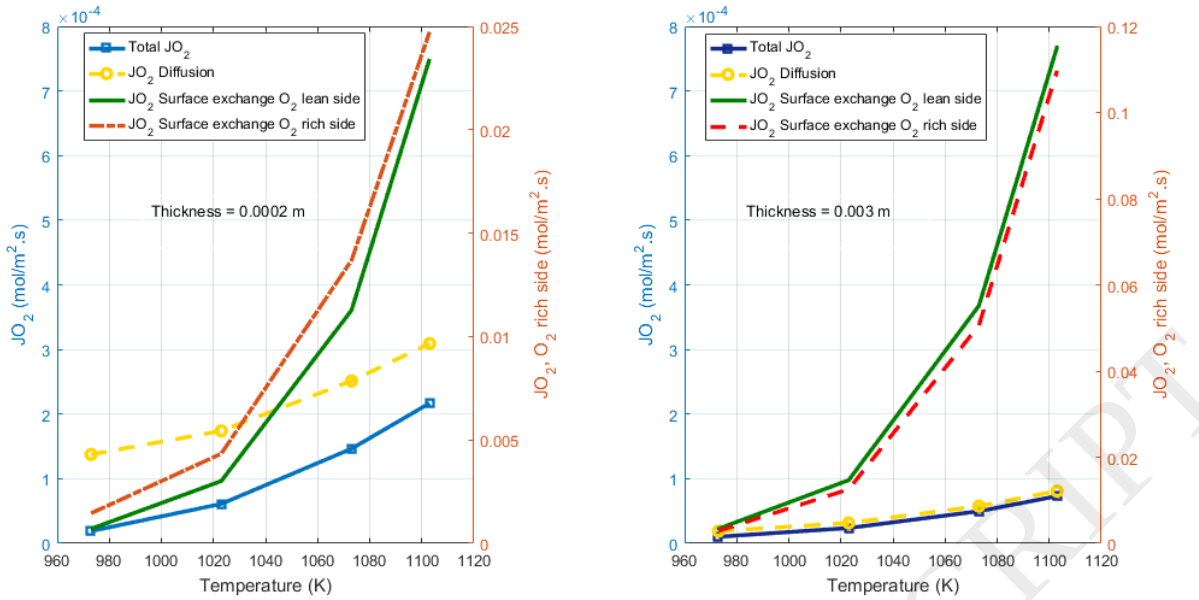


**Figure 9. Effect of temperature on $O_2$ permeation flux using the full $JO_2$-2 flux model or only one of the three considered resistances limiting at a constant membrane thickness of 0.0002 m [Left] and 0.003 m [Right].**

**Table 1. Reactor geometry, operating conditions and catalyst properties used for simulations.**

| | | | |
|---|---|---|---|
| Reactor length (m) | 0.10 | Pellet diameter (m) | $3\times10^{-4}$ |
| Tube diameter (m) | 0.01 | Catalyst density (kg $m^{-3}$) | 3600 |
| Membrane thickness (m) | 0.003[a] | Volume flow tube (STP) ($m^3\,s^{-1}$) | $1 - 5\times10^{-6}$ |
| Bed voidage (-) | 0.38 | Volume flow shell (STP) ($m^3\,s^{-1}$) | $1 - 3\times10^{-6}$ |
| Reactor pressure (bar) | 1.1 | Inlet temperature (K) | 1073[b] |

[a] Constant for MR simulations or initial value at $z = 0$ for VTMR optimisation

[b] Apart from Section 3.5 investigating temperature effect

**Table 2. Independent variables with lower and upper bounds used during optimization of the VTMR configuration. Variables refer to equation (12).**

| Variable | Lower Bound, $\beta^L$ | Upper Bound, $\beta^U$ | Initial Value |
|---|---|---|---|
| Membrane thickness, $L_{m_0}$ | 0.0001 | 0.01 | 0.003 |
| Slope of thickness, $\sigma$ | 0.00 | 1.50 | 1.00 |

**Table 3 Comparison of the performance of reactor configurations using the $JO_2$-1 flux model. Inlet composition: Tube ($O_2$ = 0.0, $CH_4$ = 0.63, $N_2$ = 0.37) and Shell ($N_2$ = 0.79 and $O_2$ = 0.21). Operating conditions: Temperature 1073 K, Pressure 1 atm and $V_R/Q_{tot,0}$ 7.85 s.**

| **Reactor configuration / Gas phase reaction network** | **$CH_4$ Conversion, %** | **$O_2$ Conversion, %** | **$C_2$ Selectivity, %** | **$C_2$ Yield, %** | **$C_2H_4/C_2H_6$ ratio** |
|---|---|---|---|---|---|
| **1D PBR/GM-2** | 27.72 | 100.0 | 29.86 | 8.28 | 6.78 |
| **2D MR/GM-2** | 24.31 | 82.91 | 47.86 | 11.63 | 3.76 |
| **2D VTMR/GM-2** | 16.73 | 91.25 | 67.26 | 11.25 | 2.54 |
| **2D VTMR/GM-2 at 0.17 m[a]** | 23.66 | 94.25 | 59.42 | 14.06 | 4.44 |

[a] VTMR performance at larger reactor length to achieve the same $CH_4$ conversion as the MR

**Table 4. Optimal values of membrane configuration in 1D VTMR in terms of $C_2$ selectivity, according to procedures described in Section 2.5, using $JO_2$-1. Inlet composition: Tube ($O_2$ = 0.0, $CH_4$ = 0.63, $N_2$ = 0.37) and Shell ($O_2$ = 0.21, $N_2$ = 0.79). Process conditions: Temperature 1073 K, Pressure = 1 atm, $V_R/Q_{tot,0}$ 7.85 s.**

| **Energy balance** | **Isothermal** | | | **Adiabatic** | |
|---|---|---|---|---|---|
| **Gas Phase model** | GM-2 | GM-1 | GM-0 | GM-2 | GM-1 |
| **Membrane thickness, $L_{m_0}$** | 0.0058 | 0.010 | 0.0099 | 0.0056 | 0.0058 |
| **slope of linear equation, $\sigma$** | 0.440 | 1.4239 | 1.4892 | 1.230 | 1.410 |

**Table 5. Comparison of 2D MR and VTMR at equal lengths and equal conversion points in an adiabatic configuration using $JO_2$-1 and GM-2. Inlet composition: Tube ($O_2$ = 0.0, $CH_4$ = 0.63, $N_2$ = 0.37) and Shell ($N_2$ = 0.79 and $O_2$ = 0.21). Operating conditions: Inlet temperature = 1073 K, Pressure = 1 atm and $V_R/Q_{tot,0}$ = 1.57 s. Optimized VTMR membrane parameters described in Table 4.**

| Reactor | Length (m) | $CH_4$ Conversion, % | $C_2$ Selectivity, % | $C_2$ Yield, % | $O_2$ Conversion, % | $C_2H_4/C_2H_6$ |
|---|---|---|---|---|---|---|
| **MR** | **0.01** | 2.96 | 80.22 | 2.37 | 41.08 | 0.08 |
| **VTMR** | **0.01** | 2.65 | 81.69 | 2.17 | 47.15 | 0.08 |
| **MR** | **0.03** | 7.93 | 65.59 | 5.20 | 79.25 | 0.63 |
| **VTMR** | **0.05** | 7.76 | 69.76 | 5.42 | 88.37 | 0.90 |
| **MR** | **0.05** | 10.55 | 53.29 | 5.62 | 84.44 | 1.63 |
| **VTMR** | **0.10** | 10.55 | 59.76 | 6.30 | 92.78 | 2.12 |
| **MR** | **0.10** | 16.91 | 30.90 | 5.23 | 89.32 | 5.40 |
| **VTMR** | **0.24** | 16.72 | 46.07 | 7.70 | 96.78 | 5.16 |